

Serendipitous Nebular-phase *JWST* Imaging of SN Ia 2021aefx: Testing the Confinement of ⁵⁶Co Decay Energy

NESS MAYKER CHEN,^{1,2} MICHAEL A. TUCKER,^{2,1,*} NILS HOYER,³ SAURABH W. JHA,⁴ LINDSEY KWOK,⁴
ADAM K. LEROY,^{1,2} ERIK ROSOLOWSKY,⁵ CHRIS ASHALL,⁶ GAGANDEEP ANAND,⁷ FRANK BIGIEL,⁸ MÉDÉRIC BOQUIEN,⁹
CHRIS BURNS,¹⁰ DANIEL DALE,¹¹ JAMES M. DERKACY,⁶ OLEG V. EGOROV,¹² L. GALBANY,^{13,14} KATHRYN GRASHA,^{15,16,†}
HAMID HASSANI,⁵ PETER HÖEFLICH,¹⁷ ERIC HSIAO,¹⁷ RALF S. KLESSEN,^{18,19} LAURA A. LOPEZ,^{1,2} JING LU,¹⁷
NIDIA MORRELL,²⁰ MARIANA ORELLANA,^{21,22} FRANCESCA PINNA,²³ SUMIT K. SARBADHICARY,^{1,2} EVA SCHINNERER,²³
MELISSA SHAHBANDEH,^{24,7} MAXIMILIAN STRITZINGER,²⁵ DAVID A. THILKER,²⁴ AND THOMAS G. WILLIAMS²⁶

¹Department of Astronomy, The Ohio State University, 140 West 18th Avenue, Columbus, Ohio 43210, USA

²Center for Cosmology and Astroparticle Physics, 191 West Woodruff Avenue, Columbus, OH 43210, USA

³Donostia International Physics Center, Paseo Manuel de Lardizabal 4, E-20118 Donostia-San Sebastián, Spain

⁴Department of Physics and Astronomy, Rutgers, the State University of New Jersey,
136 Frelinghuysen Road, Piscataway, NJ 08854, USA

⁵Department of Physics, University of Alberta, Edmonton, AB T6G 2E1, Canada

⁶Department of Physics, Virginia Tech, Blacksburg, VA 24061, USA

⁷Space Telescope Science Institute, 3700 San Martin Drive, Baltimore, MD 21218, USA

⁸Argelander-Institut für Astronomie, Universität Bonn, Auf dem Hügel 71, 53121 Bonn, Germany

⁹Centro de Astronomía (CITEVA), Universidad de Antofagasta, Avenida Angamos 601, Antofagasta, Chile

¹⁰Observatories of the Carnegie Institution for Science, 813 Santa Barbara Street, Pasadena, CA 91101, USA

¹¹Department of Physics and Astronomy, University of Wyoming, Laramie, WY 82071, USA

¹²Astronomisches Rechen-Institut, Zentrum für Astronomie der Universität Heidelberg, Mönchhofstraße 12-14, D-69120 Heidelberg,
Germany

¹³Institute of Space Sciences (ICE, CSIC), Campus UAB, Carrer de Can Magrans, s/n, E-08193 Barcelona, Spain

¹⁴Institut d'Estudis Espacials de Catalunya (IEEC), E-08034 Barcelona, Spain

¹⁵Research School of Astronomy and Astrophysics, Australian National University, Canberra, ACT 2611, Australia

¹⁶ARC Centre of Excellence for All Sky Astrophysics in 3 Dimensions (ASTRO 3D), Australia

¹⁷Department of Physics, Florida State University, 77 Chieftan Way, Tallahassee, FL 32306, USA

¹⁸Universität Heidelberg, Zentrum für Astronomie, Institut für Theoretische Astrophysik, Albert-Ueberle-Str 2, D-69120 Heidelberg,
Germany

¹⁹Universität Heidelberg, Interdisziplinäres Zentrum für Wissenschaftliches Rechnen, Im Neuenheimer Feld 205, D-69120 Heidelberg,
Germany

²⁰Las Campanas Observatory, Carnegie Observatories, Casilla 601, La Serena, Chile

²¹Universidad Nacional de Río Negro. Sede Andina, Mitre 630 (8400), Bariloche, Argentina

²²Consejo Nacional de Investigaciones Científicas y Técnicas (CONICET), Argentina

²³Max Planck Institute for Astronomy, Königstuhl 17, 69117 Heidelberg, Germany

²⁴Department of Physics and Astronomy, Johns Hopkins University, Baltimore, MD 21218, USA

²⁵Department of Physics and Astronomy, Aarhus University, Ny Munkegade 120, DK-8000 Aarhus C, Denmark

²⁶Sub-department of Astrophysics, Department of Physics, University of Oxford, Keble Road, Oxford OX1 3RH, UK

ABSTRACT

We present new 0.3 – 21 μm photometry of SN 2021aefx in the spiral galaxy NGC 1566 at +357 days after *B*-band maximum, including the first detection of any SN Ia at $> 15 \mu\text{m}$. These observations follow earlier *JWST* observations of SN 2021aefx at +255 days after the time of maximum brightness, allowing us to probe the temporal evolution of the emission properties. We measure the fraction of flux emerging at different wavelengths and its temporal evolution. Additionally, the integrated 0.3 – 14 μm decay rate of $\Delta m_{0.3-14} = 1.35 \pm 0.05 \text{ mag}/100 \text{ days}$ is higher than the decline rate from the radioactive decay of ⁵⁶Co of $\sim 1.2 \text{ mag}/100 \text{ days}$. The most plausible explanation for this discrepancy is that flux is shifting to $> 14 \mu\text{m}$, and future *JWST* observations of SNe Ia will be able to directly test this

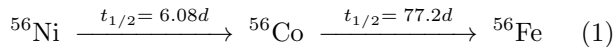
hypothesis. However, models predicting non-radiative energy loss cannot be excluded with the present data.

Keywords: interstellar medium: star-formation - supernova: locations - galaxies: nearby

1. INTRODUCTION

Type Ia supernovae (SNe Ia) are the thermonuclear explosions of carbon-oxygen white dwarf stars (Hoyle & Fowler 1960). Their importance is two-fold: their use as standard candles is essential to the field of cosmology (e.g., Schmidt et al. 1998), and they produce the majority of iron-group elements in the Universe (e.g., Iwamoto et al. 1999). Despite their overarching importance, many open questions remain regarding their progenitor systems and explosion mechanisms (see Maoz et al. 2014; Jha et al. 2019 for recent reviews).

SNe Ia are powered by the radioactive decay of unstable isotopes synthesized during the explosion (Pankey 1962). The decay of



dominates the energy deposition into the ejecta for the first ~ 3 years after explosion (e.g., Seitenzahl et al. 2009). γ -rays emitted during the first half of this decay chain, ${}^{56}\text{Ni} \rightarrow {}^{56}\text{Co}$, provide the majority of the heating at $\lesssim 200$ days after explosion (e.g., Arnett 1982; Childress et al. 2015). The second decay, ${}^{56}\text{Co} \rightarrow {}^{56}\text{Fe}$, produces X-ray and γ -ray photons in addition to high-energy (~ 1 MeV) positrons (e^+) that dominate the energy deposition $\approx 200 - 1200$ days after explosion (e.g., Kushnir & Waxman 2020; Tucker et al. 2022b).

For many years it was unclear if some of the ${}^{56}\text{Co} \rightarrow {}^{56}\text{Fe}$ decay energy escaped from the ejecta into the surrounding environment. Early studies of late-time SN Ia light curves found that the nebular-phase ($\gtrsim 150$ days after maximum light, e.g. Bowers et al. 1997; Branch et al. 2008) optical ($0.3 - 1 \mu\text{m}$) brightness declined faster than expected for the radioactive decay of ${}^{56}\text{Co}$, suggesting a fraction ($\sim 1 - 10\%$) of the decay energy was not confined to the ejecta (e.g., Milne et al. 2001). This changed with the inclusion of *JHK* ($1 - 2.5 \mu\text{m}$) observations which reconciled the (pseudo-)bolometric decline rate with expectations for pure ${}^{56}\text{Co}$ decay (e.g., Stanishev et al. 2007; Stritzinger & Sollerman 2007; Leloudas et al. 2009).

A persistent uncertainty in these studies is the unknown fraction of flux emerging at $\gtrsim 2.5 \mu\text{m}$. Gerardy et al. (2007) published single-epoch nebular-phase *Spitzer* spectra of SNe Ia 2003hv and 2005df extending to $15 \mu\text{m}$. Johansson et al. (2017) analyzed multi-epoch *Spitzer* light curves of SNe Ia extending into the nebular phase, but were limited to the CH1 ($3.6 \mu\text{m}$) and CH2

($4.5 \mu\text{m}$) bandpasses. Kwok et al. (2022) and DerKacy et al. (2023) recently published spectra of SN 2021aefx extending to $14 \mu\text{m}$ with *JWST* at +255 and +323 days after maximum light, respectively. SN 2014J has multiple mid-IR spectra (Telesco et al. 2015) with the caveat that the spectra were obtained from the ground with the Gran Telescopio Canarias, where the high sky brightness and low atmospheric transmission in the mid-IR complicates precise flux calibration. To date, no SN Ia has been detected at $> 15 \mu\text{m}$. Three SNe Ia (2011by, 2011fe, and 2012cg) were observed within 45 days of maximum light with *Herschel* at $70 \mu\text{m}$ and $160 \mu\text{m}$, but only upper limits were obtained (Johansson et al. 2013).

In this Letter, we report new optical and IR broadband imaging of SN 2021aefx at +357 days after *B*-band maximum light. The new *JWST* data were obtained as part of the Physics at High Angular Resolution of Nearby Galaxies (PHANGS)-*JWST* Cycle 1 Treasury Program (Lee et al. 2022), which observed the host of SN 2021aefx, NGC 1566, in eight filters spanning $2 - 21 \mu\text{m}$ (*F200W* to *F2100W*). While the core science goals of PHANGS-*JWST* center on understanding stellar formation and feedback in nearby, star-forming galaxies, the serendipitous $2-21 \mu\text{m}$ observations of SN 2021aefx provide new insight into the cooling properties of SN Ia ejecta at nebular phases, including the first detection of a SN Ia at $> 15 \mu\text{m}$.

SN 2021aefx was discovered on November 11, 2021 (MJD 59529, Valenti et al. 2021; Bostroem et al. 2021) by the Distance Less Than 40 Mpc (DLT40) transient survey (Tartaglia et al. 2018). Its host galaxy, NGC 1566, is a massive ($\log_{10} M_{\star} [M_{\odot}] \approx 10.8$), relatively face-on star-forming (SFR $\approx 4.5 M_{\odot} \text{ yr}^{-1}$) spiral galaxy (Leroy et al. 2021) at a distance $d = 17.69 \pm 2.02$ Mpc (distance modulus $\mu = 31.24 \pm 0.27$ mag) (Kourkchi & Tully 2018; Anand et al. 2021) and redshift $z = 0.00502 \pm 0.00001$ (Allison et al. 2014). Despite excess *u*-band emission in the early light curve (Ashall et al. 2022), SN 2021aefx evolved into a normal SN Ia with $\Delta m_{15}(B) = 0.90 \pm 0.02$ mag and reached $M_B = -19.63 \pm 0.02$ mag on $t_{\text{max}} = \text{MJD } 59546.5$ (Hosseinzadeh et al. 2022).

The brightness and close proximity of SN 2021aefx make it an excellent target for nebular-phase *JWST* observations. Kwok et al. (2022) and DerKacy et al. (2023) provided the first demonstration of the impressive spectroscopic capabilities of *JWST* for studying nebular-phase SNe Ia. Their spectra of SN 2021aefx, obtained +255 days and +323 days after t_{max} , respectively, represent the highest-quality look at the emission properties $> 2.5 \mu\text{m}$ of SNe Ia to date. Their spectra show prominent emission features from the iron-group elements (Ni,

* CCAPP Fellow

† ARC DECRA Fellow

Co, Fe), as well as a wide, flat-topped [Ar III] profile that indicates a spherical shell of emission.

Our new 2 – 21 μm *JWST* photometry at +357 days are used in conjunction with the +255 day 0.3 – 14 μm spectrum from [Kwok et al. \(2022\)](#) to 1) provide the time-dependent fraction of flux emerging at optical, near-IR, and mid-IR wavelengths; and 2) determine if the decline rate of the 0.3 – 14 μm flux is consistent with expectations for the radioactive decay of $^{56}\text{Co} \rightarrow ^{56}\text{Fe}$. The imaging data and reduction are described in §2. §3 outlines our analysis procedure, including constructing the 2–21 μm SED (Figure 2) and calculating filter-specific and bolometric decay rates (Figure 3 and Table 2). Finally, in §4 we discuss and summarize our results.

2. OBSERVATIONS

2.1. Near- and Mid-IR Photometry

JWST ([Rigby et al. 2022](#)) observed NGC 1566 on November 22, 2022 (MJD 59905.4) using both the near-infrared camera instrument (NIRCam, [Rieke et al. 2022](#)) and mid-infrared instrument (MIRI, [Rieke et al. 2015](#); [Wright et al. 2015](#)) as part of the PHANGS-*JWST* Treasury survey (GO program 2107, PI: J. Lee; [Lee et al. 2022](#)). The observations include NIRCam imaging using the *F200W*, *F300M*, *F335M*, and *F360M* filters and MIRI imaging using the *F770W*, *F1000W*, *F1130W*, and *F2100W* filters. [Lee et al. \(2022\)](#) describe the general procedures for PHANGS-*JWST* observations and reduction. Here we use a preliminary version of the images reduced with the Calibration References Data System¹(CRDS) version 11.16.15 (NIRCam) and 11.16.16 (MIRI).

Figure 1 shows the location of SN 2021aefx in NGC 1566 and presents cutouts around this location in each filter. The figure shows that in all eight filters, SN 2021aefx appears as a bright point source near the J2000 location of $\alpha = 64.9725^\circ$ and $\delta = -54.948081^\circ$ reported by [Valenti et al. \(2021\)](#). Despite the significant variation of the PSF size from 2 to 21 μm , there is no issue identifying the location of the source in each band, and the SN always appears brighter than the surrounding emission.

We measure the flux of SN 2021aefx using aperture photometry and report our results in Table 1. To do this, we use the aperture photometry module of the ASTROPY-affiliated package PHOTUTILS². Because we use initial versions of the PHANGS-*JWST* images in which the astrometry remains moderately uncertain, we center the circular aperture on the brightest pixel associated with the SN, which is slightly offset from filter to filter. We have no reason to think that the position of the SN

varies by band and ascribe all of the slight variations in position to astrometric uncertainty.

We assign aperture radii of 2 times the full width at half maximum (FWHM) of the point spread function (PSF) for each filter. We also estimate and subtract a local background using an annulus spanning from 1.5 to 3 times the radius of this photometric aperture (Figure 1). Finally, we apply an aperture correction to each filter based on the fraction of total energy encircled within the PSF (found using WebbPSF³; [Perrin et al. 2015](#)) of our adopted aperture.

We check our photometry by also estimating the flux using two independent methods. The first follows [Hoyer et al. \(2022\)](#) and fits the source with two Sérsic profiles, one for the core and another for the halo of the source, without PSF convolution. The two profiles are integrated to find the total flux of the source, and a flat offset is added to account for the background. The second check uses the DOLPHOT stellar photometry package ([Dolphin 2000, 2016](#)), which estimates the flux of sources using PSF-fitting applied to individual calibrated image frames (“level 2”) prior to drizzling the images into the final mosaics used for our primary analysis (“level 3”). Our DOLPHOT analysis uses the beta versions of the NIRCam⁴ ([Weisz et al. in prep.](#)) and MIRI⁵ ([Peltonen et al. in prep.](#)) modules. These measurements differ by an average of 6% from our nominal flux density measurement.

We also estimate statistical and systematic uncertainties associated with the photometry.

We use a relatively empty region of the image itself to assess the statistical uncertainty. To do this we focus on the northwest corner of the image, which is free of bright emission (Figure 1). For each band, we generate 100 apertures with the same radius as the measurement aperture for that band, and place them randomly in the empty region. We then measure the standard deviation amongst the flux measurements for these empty apertures and treat this as a realistic estimate of the statistical uncertainty. Because both the local background and the source measurement varies across these “empty” apertures, we expect this estimate to reflect both uncertainty in the background level and noise within the aperture.

We include two contributions to the systematic uncertainty of each measurement, an overall flux calibration uncertainty and a methodological uncertainty. For the first, we assume a 4% overall calibration uncertainty because *JWST* targets an overall flux calibration of 2%⁶ and [Rigby et al. \(2022\)](#) quote a photometric re-

¹ <https://jwst-crds.stsci.edu/>

² <https://photutils.readthedocs.io/en/stable/aperture.html>

³ <https://webbpsf.readthedocs.io/en/stable/index.html>

⁴ <http://americano.dolphinim.com/dolphot/nircam.html>

⁵ <http://americano.dolphinim.com/dolphot/miri.html>

⁶ <https://jwst-docs.stsci.edu/jwst-data-calibration-considerations/jwst-data-absolute-flux-calibration>

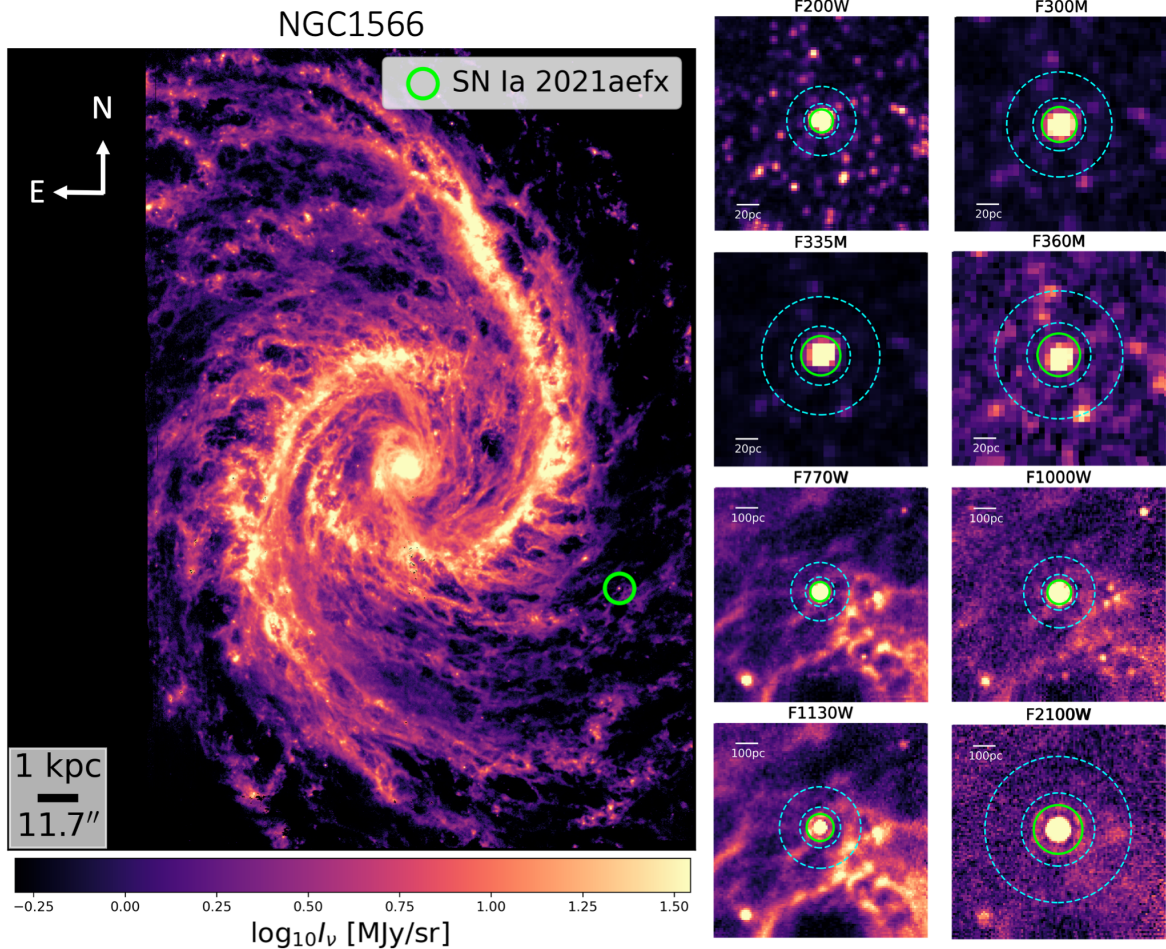


Figure 1. *SN 2021aefx* in *NGC 1566* at $\approx 2\text{--}21\mu\text{m}$. Left panel: MIRI *F1130W* PHANGS-JWST image of *NGC 1566* showing the location of *SN 2021aefx* marked with a green circle. Right panels: zoom-ins on *SN 2021aefx* in each PHANGS-JWST filter. The top four panels show $200\text{ pc} \times 200\text{ pc}$ cutouts from NIRCcam images at $2.0\text{--}3.6\mu\text{m}$. The bottom four panels show $1\text{ kpc} \times 1\text{ kpc}$ MIRI images at $7.7\text{--}21\mu\text{m}$. The inner green circle marks the aperture used in the photometry measurement, and the two concentric, dashed, cyan circles mark the inner and outer apertures used for the background subtraction. The results of the photometry appear in Table 1.

producibility of 4% for NIRCcam. To be conservative, we assume that this 4% value reflects the current calibration uncertainty of the telescope, and that this also applies to MIRI imaging. The second, methodological term reflects that different methods that ideally should yield identical results vary due to the influence of the background, imperfect knowledge of the PSF, or other methodological choices. To account for this, we take the median absolute deviation among the three flux measurements obtained with different methods for each filter, and then express this as a corresponding RMS uncertainty. Finally, we add both systematic uncertainties

in quadrature and report them alongside the statistical uncertainty in Table 1.

Table 1 also reports νL_ν and $\Delta\nu L_\nu$, calculated by converting the flux density to a luminosity (L_ν) and then multiplying by the frequency at the nominal filter center^{7 8}, ν , and the nominal frequency width of the filter, $\Delta\nu$, respectively. $\Delta\nu L_\nu$ is a more useful physical measurement than νL_ν because it more nearly corresponds

⁷ <https://jwst-docs.stsci.edu/jwst-near-infrared-camera>

⁸ <https://jwst-docs.stsci.edu/jwst-mid-infrared-instrument>

Table 1. Filter specific photometry data: exposure time, t ; nominal wavelength at the filter center, λ ; nominal wavelength width of the filter, $\Delta\lambda$; flux density, Flux; statistical uncertainty, σ_{Stat} ; systematic uncertainty, σ_{Sys} ; Luminosity times the frequency νL_ν ; and Luminosity times the nominal frequency width of the filter $\Delta\nu L_\nu$

Filter	t	λ	$\Delta\lambda$	Flux	σ_{Stat}	σ_{Sys}	νL_ν	$\Delta\nu L_\nu$
	[s]	[μm]	[μm]	[μJy]	[μJy]	[μJy]	[$10^5 L_\odot$]	[$10^5 L_\odot$]
F200W	1203	1.99	0.461	20.12	1.55	0.85	3.012	0.707
F300M	387	2.996	0.318	14.2	0.15	1.45	1.412	0.15
F335M	387	3.365	0.347	19.28	0.21	1.67	1.707	0.176
F360M	430	3.621	0.372	4.77	0.2	0.2	0.392	0.04
F770W	88	7.7	2.2	268.52	1.39	26.34	10.388	3.03
F1000W	122	10.0	2.0	173.33	1.41	25.38	5.163	1.043
F1130W	311	11.3	0.7	181.41	2.3	11.24	4.782	0.297
F2100W	321	21.0	5.0	440.26	7.36	22.51	6.245	1.508

to a direct integral over the filter⁹, and the emission from the SN is expected to be localized line emission (e.g., Fransson & Jerkstrand 2015; Kwok et al. 2022).

2.2. Flux Calibration of the +255 day Spectrum

We compute synthetic photometry from the 0.3 – 14 μm +255 day spectrum of SN 2021aefx published by Kwok et al. (2022) so we briefly discuss the precision of the spectral flux calibration. *JWST* is currently obtaining Cycle 1 calibration observations so the absolute flux calibration has not been finalized. However, there are several reasons why we consider the flux calibration of the +255 day spectrum to be sufficient. The optical portion of the +255 day spectrum has contemporaneous *UBgVri* photometry to ensure precise flux calibration (Kwok et al. 2022). Additionally, the MIRI Low-Resolution Spectroscopy (LRS) spectrum is scaled by only 2% to match the MIRI *F1000W* acquisition-image photometry (Kwok et al. 2022). Thus, the optical and mid-IR wavelengths have flux calibration accurate to $\lesssim 5\%$.

Only the NIRSpec observations lack corresponding photometry. While this could result in uncertain flux calibration for the $\approx 1 - 5 \mu\text{m}$ range, the NIRSpec spectrum shows excellent agreement with the flux-calibrated optical and mid-IR spectra on either end of the wavelength range. The current *JWST* flux calibration is accurate to 2 – 5% (S. Kendrew, private comm.) so we adopt a conservative uncertainty of 0.1 mag for photom-

etry synthesized from the NIRSpec (1 – 5 μm) portion and 0.05 mag otherwise.

2.3. Optical Photometry

We supplement the *JWST* observations with optical *BVgri* imaging from the Precision Observations of Infant Supernova Explosions (POISE; Burns et al. 2021) project. These observations were conducted on MJD 59904.7, ≈ 17 rest-frame hours before the *JWST* observations, with the SITE3 camera on the Swope telescope. Section 2 in Ashall et al. (2022) provides a brief overview of the data reduction and calibration process with further discussions in Krisciunas et al. (2017). Finally, difference imaging with SkyMapper (Wolf et al. 2018) data is used to mitigate the host-galaxy contribution although the effect is minimal for SN 2021aefx as it is located in the outskirts of NGC 1566.

3. RESULTS

Figure 2 shows our new near- and mid-IR photometry of SN 2021aefx at +357 days after maximum light. Our new measurements appear as purple stars, with the filters illustrated below the SED and the nominal filter widths indicated by the horizontal error bars. Filter curves are taken from the Spanish Virtual Observatory’s filter profile service¹⁰ (Rodrigo & Solano 2020). The solid line behind our data shows the spectrum of Kwok et al. (2022). For comparison, we also compute synthetic photometry from the +255 day 0.3 – 14 μm spectrum of SN 2021aefx (Kwok et al. 2022), which appears as black-and-white circles.

⁹ This approach neglects second order effects related to the locations of the lines and the spectral slope adopted during calibration. When comparing to the Kwok et al. (2022) spectral data below we impute synthetic photometry from their spectra to allow a rigorous comparison.

¹⁰ <http://svo2.cab.inta-csic.es/theory/fps3/>

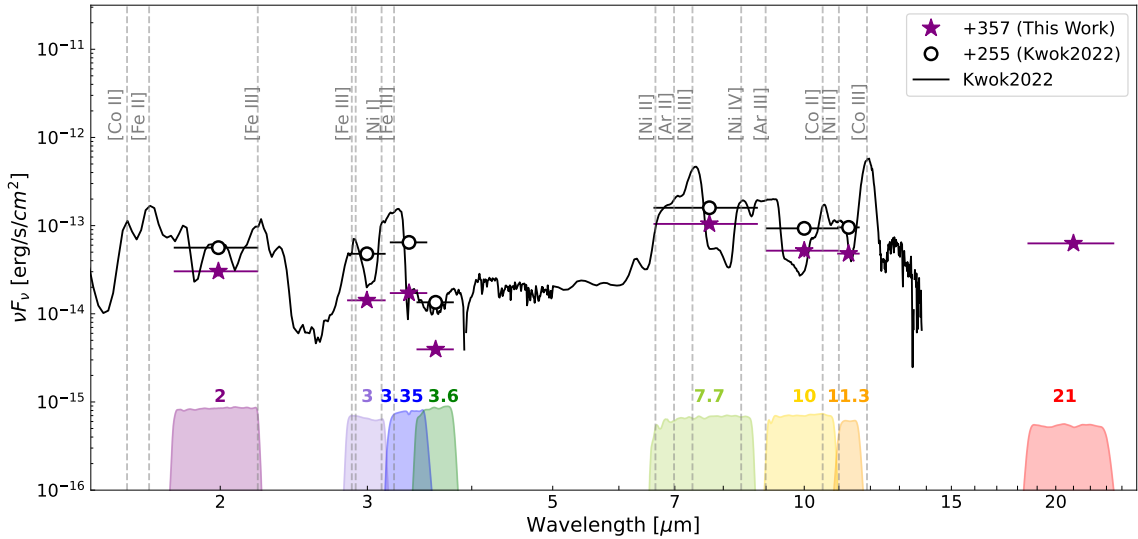


Figure 2. A comparison of the Near- and Mid- IR flux of SN 2021aefx at +255 and +357 days. Purple stars mark our flux measurements from each filter and black open circles signify synthetic photometry from the +255-day spectrum (black line). Horizontal error bars show the nominal wavelength width of each filter. Vertical error bars mark the uncertainty in the measurement and are shown, but are typically smaller than the points. The vertical grey dashed lines mark emission features identified by Kwok et al. (2022). NIRCam and MIRI filter curves are plotted along the bottom axis.

Comparing the synthesized photometry to the new *JWST* observations, one can see that the shape of the SED measured from our data resembles that found by Kwok et al. (2022). While SN 2021aefx has faded slightly during the ≈ 102 days between these observations, the dominant emission features appear to have similar strengths with the exception of Co-dominated features (DerKacy et al. 2023) as ^{56}Co decays into ^{56}Fe . This is consistent with the optical and near-IR spectroscopic evolution of SNe Ia during this time span (e.g., Mazzali et al. 2020; Tucker et al. 2022a; Graham et al. 2022).

Our $F2100W$ detection is unique because it was not covered by the spectrum obtained by Kwok et al. (2022). No models in the literature currently predict which emission features should be present at these wavelengths. Fransson & Jerkstrand (2015) suggest that several MIR fine-structure lines dominate the total emission of SN 2011fe at ~ 1000 days after t_{max} , but time-dependent modeling is unavailable. Thus, we use simple assumptions to estimate the emission features responsible for the observed $F2100W$ flux.

The temperature and electron density at these epochs are $T_e \approx 10^4$ K and $\log_{10}(n_e[\text{cm}^{-3}]) \approx 5 - 6$ (e.g., Fransson & Jerkstrand 2015; Flörs et al. 2020; Shingles et al. 2022). The ground-state [Fe III] 22.93 μm transition likely accounts for most of the observed flux despite the $F2100W$ bandpass capturing only $\sim 50\%$ of the total emission. The rest of the observed flux might be attributable to a combination of the weaker

[Ar III] 21.83 μm and [Co II] 18.80 μm lines, although detailed modeling is needed to accurately capture the complex non-LTE processes at nebular epochs (e.g., Li et al. 2012; Shingles et al. 2020; Hoefflich et al. 2021). Future observations with the *JWST* MIRI Mid-Resolution Spectrometer (MRS; Wells et al. 2015) will directly measure the contributing spectral features.

Combining the flux-calibrated +255 day spectrum with our new optical and IR photometry, we estimate the fraction of flux emerging in the optical, near-IR, and mid-IR for both epochs. The $F2100W$ measurement is excluded from these calculations due to the uncertain spectral shape as SNe Ia are dominated by line emission at nebular epochs. The +255 day spectrum is scaled to match the observed +357 day optical and IR photometry using the filter-specific decline rates shown in Figure! 3. A bootstrapping routine is used to estimate the associated uncertainty. For the 1 – 2 μm region where we lack corresponding photometry, the J - and H -band decline rate is uniformly sampled between 0.0 – 0.3 mag/100 days which was found for a sample of SNe Ia by Graur et al. (2020). The final scaled spectrum and its uncertainty are shown in Figure 4. The fraction of 1 – 2.5 μm to 0.3 – 1 μm flux is $5.1 \pm 0.5\%$ and $13.4 \pm 1.3\%$ at +255 and +357 days, respectively, in agreement with previous estimates for other SNe Ia (Stanishev et al. 2007; Leloudas et al. 2009; Dimitriadis et al. 2017; Maguire et al. 2018; Graur et al. 2020). We consider this agreement, without adopting prior assumptions on the optical to near-IR flux ratios, a general con-

Table 2. Integrated fluxes F and fractional contribution to the total $0.3 - 14 \mu\text{m}$ flux f for different wavelengths. Fractions may not exactly equal 100% due to round-off and sampling errors.

λ	F_{255}	f_{255}	F_{357}	f_{357}	Δm
$[\mu\text{m}]$	$[\text{erg s}^{-1} \text{cm}^{-2}]$	$[\%]$	$[\text{erg s}^{-1} \text{cm}^{-2}]$	$[\%]$	$[\text{mag}/100 \text{days}]$
0.3 – 1	$(1.3 \pm 0.1) \times 10^{-12}$	86.1 ± 3.9	$(3.0 \pm 0.2) \times 10^{-13}$	72.0 ± 4.6	1.57 ± 0.04
1 – 2.5	$(6.9 \pm 0.3) \times 10^{-14}$	4.7 ± 0.3	$(4.6 \pm 0.4) \times 10^{-14}$	11.3 ± 1.0	0.43 ± 0.08
2.5 – 5	$(2.1 \pm 0.1) \times 10^{-14}$	1.4 ± 0.1	$(5.6 \pm 0.8) \times 10^{-15}$	1.4 ± 0.2	1.42 ± 0.15
5 – 14	$(1.1 \pm 0.1) \times 10^{-13}$	7.5 ± 0.4	$(6.0 \pm 0.5) \times 10^{-14}$	14.9 ± 1.4	0.63 ± 0.08
0.3 – 14	$(1.5 \pm 0.1) \times 10^{-12}$...	$(4.1 \pm 0.2) \times 10^{-13}$...	1.35 ± 0.05

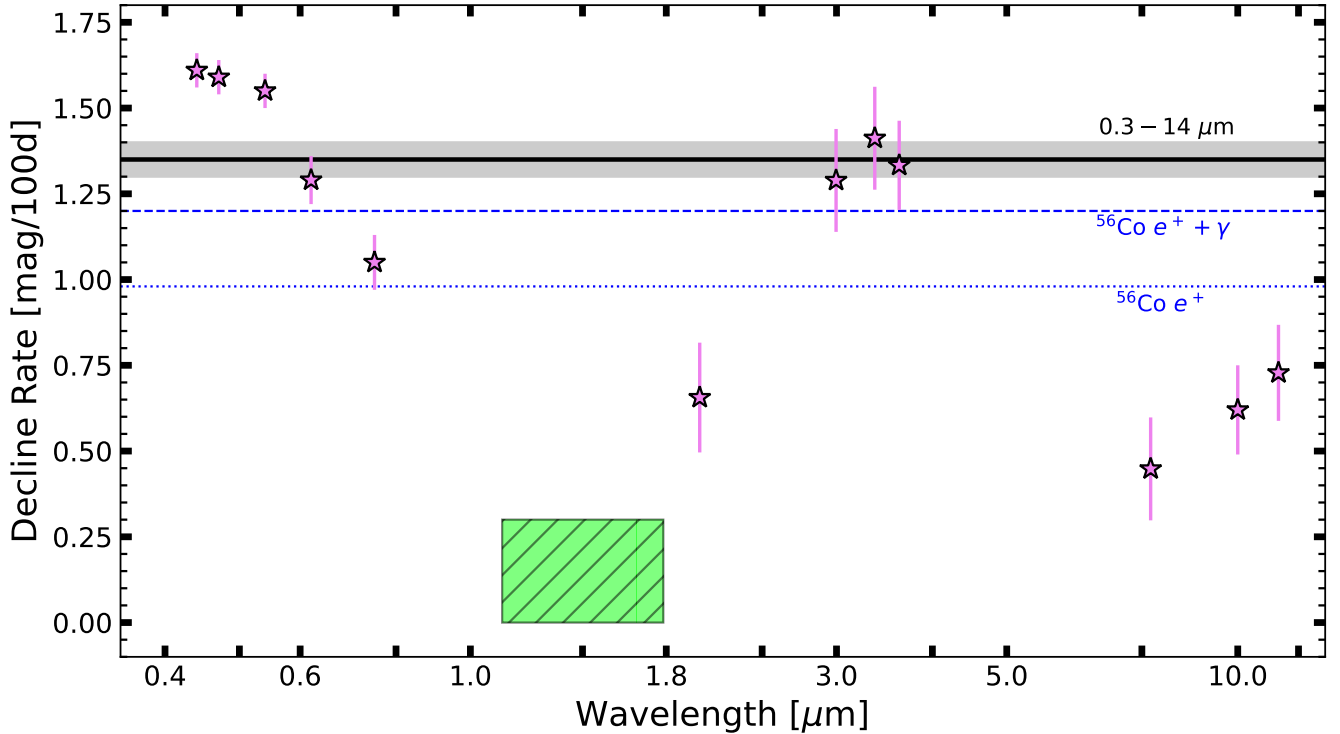


Figure 3. Nebular-phase decline rates as a function of wavelength for SN 2021aefx. The green region represents the J - and H -band decay rates of $0.0 - 0.3 \text{ mag}/100 \text{ days}$ from [Graur et al. \(2020\)](#). Blue horizontal lines show the energy deposition rate for ^{56}Co with (dashed) and without (dotted) including the γ -ray contribution. The black line and shaded region represent the integrated $0.3 - 14 \mu\text{m}$ decline rate derived in §3. Data for this figure are included in the online version of the manuscript.

firmation that our methodology is accurate within our quoted uncertainties.

Table 2 provides the fluxes for each wavelength region in addition to the fraction of the total $0.3 - 14 \mu\text{m}$ flux. The majority of the total flux is emitted at $< 1 \mu\text{m}$ for both epochs, although the relative fraction decreases from $f_{\text{opt}} \approx 85\% \rightarrow 70\%$. This decrease is compensated by the increasing fractional flux at $1 - 2.5 \mu\text{m}$ and $5 - 14 \mu\text{m}$. The $2.5 - 5 \mu\text{m}$ region appears to retain the same fraction of the total flux between the two epochs, although this spectral region only consists of $\approx 1.5\%$ of the total flux.

Finally, we use the integrated fluxes to compute the decline rates for the different wavelength regions listed in Table 2. We find that the majority of the emitted energy occurs at optical wavelengths, and this wavelength region also declines the fastest due to higher-energy transitions becoming harder to populate as the density decreases. The $\approx 3 - 4 \mu\text{m}$ region also declines quickly due to the presence of $[\text{Fe III}]$ emission features. Spectral regions corresponding to singly-ionized transitions ($1 - 2.5 \mu\text{m}$, $6 - 12 \mu\text{m}$) decline slower at $\lesssim 0.6 \text{ mag}/100 \text{ days}$, in agreement with the findings of [Gerardy et al. \(2007\)](#) and [McClelland et al. \(2013\)](#). However, the fast-declining optical wavelengths domi-

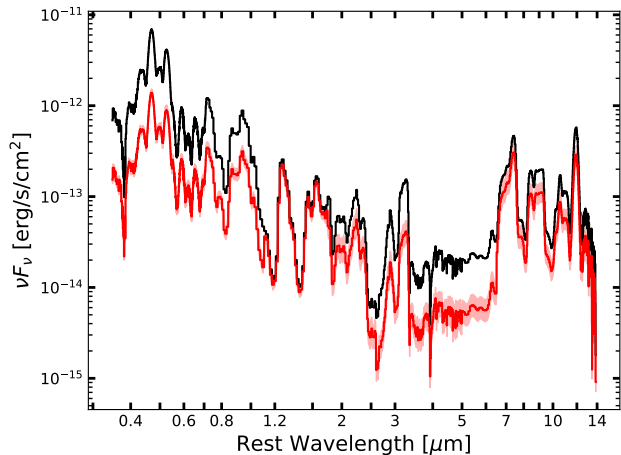


Figure 4. Flux-calibrated +255 day spectrum from Kwok et al. (2022) (black) and our reconstructed +357 day spectrum (red). The shaded region represents the 95% confidence interval from the bootstrapping routine.

nate the total flux producing a total $0.3 - 14 \mu\text{m}$ decline rate of $\Delta m_{0.3-15} = 1.35 \pm 0.05 \text{ mag}/100 \text{ days}$. This is higher than the decay rate of $0.98 \text{ mag}/100 \text{ days}$ from ^{56}Co positrons. Including the small amount of heating from singly-scattered γ -ray photons (e.g., Eq. 1 from Kushnir & Waxman 2020) raises the predicted decline rate to $1.20 \text{ mag}/100 \text{ days}$ which still disagrees with our observed decline rate at $\sim 3\sigma$.

4. DISCUSSION

We have provided new nebular-phase optical and IR imaging of the SN Ia 2021aefx, including the first detection of a SN Ia at $> 15 \mu\text{m}$. Only a few SNe Ia have mid-IR observations so comparisons are limited. However, the general picture outlined by Fransson & Jerkstrand (2015) and Graur et al. (2020) appears robust. In this picture, ultraviolet flux from Fe transitions is redistributed into the optical and IR via multiple scatterings and fluorescence (e.g., Pinto & Eastman 2000). Spectral regions corresponding to doubly-ionized transitions typically decay faster than their singly-ionized counterparts due to the ejecta cooling as it expands (e.g., McClelland et al. 2013). However, this framework for interpreting the observed decline rates may be overly simplistic as the pseudo-continuum is produced by a multitude of overlapping spectral features (e.g., Fransson & Jerkstrand 2015; Mazzali et al. 2015; Wilk et al. 2020), which may or may not evolve similarly to the strongest emission feature in a given bandpass.

The derived (pseudo-)bolometric decay rate of $1.35 \pm 0.05 \text{ mag}/100 \text{ days}$ is higher than expected for ^{56}Co decay. The most likely explanation for this discrepancy is that more flux is emerging at $> 14 \mu\text{m}$ at later epochs. [Fe II] has two low-energy transitions at $24.52 \mu\text{m}$ and $25.99 \mu\text{m}$ with lower-level energies of $E_l = 0.30 \text{ eV}$ and

$E_l = 0.00 \text{ eV}$, respectively. The nebular-phase J - and H -band plateaus are driven by low-energy [Fe II] transitions at $1 - 2 \mu\text{m}$, so it is plausible that the mid-IR transitions experience a similar flattening in the decline rate. If there is no non-radiative energy loss at these epochs (i.e., the bolometric light curve follows the energy generation rate), then the flux at $> 14 \mu\text{m}$ must have a decline rate of $\approx 0.1 \text{ mag}/100 \text{ days}$ to reconcile our results with predictions for ^{56}Co decay.

Although we find flux emerging at $> 14 \mu\text{m}$ the most plausible explanation, there are other physical processes that can expedite the (pseudo-)bolometric decay relative to ^{56}Co . Allowing a few percent of the high-energy positrons to escape the ejecta into the surrounding environment will increase the nebular-phase decline rate. In this scenario, the bolometric light curve does not reflect the energy deposition rate as some of the radioactive decay energy is not converted into photons. Magnetic fields can restrict the propagation of positrons within the ejecta but the source and strength of such fields remain unclear (e.g., Hristov et al. 2018). Furthermore, the fraction of escaping positrons would need to increase between +255 and +357 days, which is possible if the magnetic field strength diminishes as the density decreases. Allowing even a small fraction of positrons to escape the ejecta would have important ramifications for our understanding of the 511 keV positronium annihilation signal observed in the Milky Way (e.g., Siegert et al. 2016). Conversely, complete positron confinement requires a relatively strong ($\gtrsim 10^6 \text{ G}$) and/or morphologically complex magnetic field (e.g., Table 2 from Hristov et al. 2021). Strong magnetic fields can be produced in the merger of two white dwarfs (e.g., Williams et al. 2022) but it is unclear how the magnetic field strength and morphology will be affected by the explosion (e.g., Remming & Khokhlov 2014). Alternatively, particle streaming instabilities can generate magnetic fields (e.g., Gupta et al. 2021), but no simulations have assessed if nebular-phase SNe Ia ejecta meet the required instability criteria.

Separately, Kushnir & Waxman (2020) propose that the expansion of the ejecta will extend the time over which ^{56}Co positrons deposit their energy into the ejecta. This “delayed deposition” effect should result in a steepening of the light curve (relative to ^{56}Co decay) at $\lesssim 500 \text{ days}$ after t_{max} due to the finite time needed for positrons to deposit their energy into the ejecta. The deviation from ^{56}Co decay is only a few percent of the energy generation rate at $\sim 200 - 400 \text{ days}$ after t_{max} which can qualitatively reproduce our pseudo-bolometric decline rate. However, these epochs correspond to a flattening in the differential heating rate (see Figure 4 in Kushnir & Waxman 2020) which may negate any deviations from ^{56}Co decay during our observational baseline.

Future observations of SNe Ia with *JWST* are crucial to better understand the complex physics govern-

ing SNe Ia at nebular phases. Multi-epoch photometry constrains the mass ratios of isotopes produced during high-density burning (e.g., Shappee et al. 2017; Kerzendorf et al. 2017). The late-time ($\gtrsim 500$ days after t_{\max}) mid-IR luminosity is a key diagnostic of the ejecta’s cooling properties, as these epochs correspond to the end of the H -band light curve plateau (Graur et al. 2020) and a distinct shift in the optical ionization properties (Tucker et al. 2022a). Several lines of evidence suggest clumping is present in SN Ia ejecta (e.g., Black et al. 2016; Mazzali et al. 2020) but specifics about the physical conditions remain elusive (e.g., Wilk et al. 2020; Shingles et al. 2022). Emission-line profiles in the near- and mid-IR should be able to directly ascertain the nebular-phase magnetic field strength (Penney & Hoeflich 2014) and further constrain positron propagation (or lack thereof) within the ejecta (e.g., Hristov et al. 2021).

JWST is poised to revolutionize our understanding of SNe Ia in the nebular phase with both dedicated SN Ia programs (e.g., GO 2072, PI: Jha; GO 2114, PI: Ashall) and serendipitous observations like those presented here. To date, the PHANGS-JWST program has observed six nearby star-forming galaxies (IC 5332, NGC 0628, NGC 1365, NGC 1385, NGC 1566, NGC 7496). Of those galaxies, two have confirmed SNe Ia in the *JWST* footprint that exploded within the past 20 years: SN 2010el (SN Iax, Foley et al. 2013) and SN 2021aefx in NGC 1566 and SN 2012fr in NGC 1365. SN 2021aefx is analyzed here. SN 2010el is located coincident to heavy background emission in the MIRI filters and is not visible in any of the available filters (e.g., Table 1). Similarly, there is no obvious emission seen at the location of SN 2012fr. These results are unsurprising because the *JWST* images were obtained 9.75 years after t_{\max} (Contreras et al. 2018) for SN 2012fr and ~ 12.5 years after the discovery (Monard 2010) of SN 2010el.

The PHANGS-JWST Cycle 1 Treasury Program will be observing 13 more galaxies in addition to those listed above and we will continue searching for SN emission in future PHANGS data. Even the SNe that do not show clear nebular-phase emission offer an unprecedented, sharply resolved view of the environments into which SNe deposit their energy and momentum. Looking at the IR emission at the locations of these SNe can be used to constrain the late-time impact of these explosions and assess their role in the evolution of the ISM (e.g., Mayker Chen et al. 2022).

Facilities: *JWST* (NIRCam, MIRI), Swope (SITE3)

Software: Astropy (Astropy Collaboration et al. 2013), photutils (Bradley et al. 2020), Jupyter (Kluyver et al. 2016)

This work was carried out as part of the PHANGS collaboration.

AKL and NMC gratefully acknowledge support by grants 1653300 and 2205628 from the National Science Foundation, award JWST-GO-02107.009-A, award SOSP SOSPADA-010 from the NRAO, and by a Humboldt Research Award from the Alexander von Humboldt Foundation.

ER acknowledges the support of the Natural Sciences and Engineering Research Council of Canada (NSERC), funding reference number RGPIN-2022-03499 and the support of the Canadian Space Agency (CSA) [22JWGO1- 20].

JD, CA, and PH acknowledge support by NASA grant JWST-GO-02114.032-A.

MB acknowledges support from FONDECYT regular grant 1211000 and by the ANID BASAL project FB210003.

FB acknowledges funding from the European Research Council (ERC) under the European Union’s Horizon 2020 research and innovation programme (grant agreement No.726384/Empire).

OE gratefully acknowledge funding from the Deutsche Forschungsgemeinschaft (DFG, German Research Foundation) in the form of an Emmy Noether Research Group (grant number KR4598/2-1, PI Kreckel).

ES acknowledges funding from the European Research Council (ERC) under the European Union’s Horizon 2020 research and innovation programme (grant agreement No. 694343).

L.G. acknowledges financial support from the Spanish Ministerio de Ciencia e Innovación (MCIN), the Agencia Estatal de Investigación (AEI) 10.13039/501100011033, and the European Social Fund (ESF) ”Investing in your future” under the 2019 Ramón y Cajal program RYC2019-027683-I and the PID2020-115253GA-I00 HOSTFLOWS project, from Centro Superior de Investigaciones Científicas (CSIC) under PIE 20215AT016 and LINKA20409 projects, and the program Unidad de Excelencia María de Maeztu CEX2020-001058-M.

M.O. acknowledges support from UNRN PI2020 40B885.

M.D. Stritzinger is funded by the Independent Research Fund Denmark (IRFD, grant number 10.46540/2032-00022B).

This work is based on observations made with the NASA/ESA/CSA James Webb Space Telescope. The data were obtained from the Mikulski Archive for Space Telescopes at the Space Telescope Science Institute, which is operated by the Association of Universities for Research in Astronomy, Inc., under NASA contract NAS 5-03127 for JWST. These observations are associated with programs #02107 and #02072. The specific observations for PHANGS-JWST can be accessed via [10.17909/9bdf-jn24](https://archive.stsci.edu/jwst/jwst-obs/jwst-obs-02107-02072).

ACKNOWLEDGMENTS

REFERENCES

- Allison, J. R., Sadler, E. M., & Meekin, A. M. 2014, *MNRAS*, 440, 696
- Anand, G. S., Lee, J. C., Van Dyk, S. D., et al. 2021, *MNRAS*, 501, 3621
- Arnett, W. D. 1982, in *NATO Advanced Study Institute (ASI) Series C, Vol. 90, Supernovae: A Survey of Current Research*, ed. M. J. Rees & R. J. Stoneham, 221–251
- Ashall, C., Lu, J., Shappee, B. J., et al. 2022, *ApJL*, 932, L2
- Astropy Collaboration, Robitaille, T. P., Tollerud, E. J., et al. 2013, *A&A*, 558, A33
- Black, C. S., Fesen, R. A., & Parrent, J. T. 2016, *MNRAS*, 462, 649
- Bostroem, K. A., Jha, S. W., Randriamampandry, S., et al. 2021, *Transient Name Server Classification Report*, 2021-3888, 1
- Bowers, E. J. C., Meikle, W. P. S., Geballe, T. R., et al. 1997, *MNRAS*, 290, 663
- Bradley, L., Sipőcz, B., Robitaille, T., et al. 2020, *astropy/photutils: 1.0.0*, doi:10.5281/zenodo.4044744
- Branch, D., Jeffery, D. J., Parrent, J., et al. 2008, *PASP*, 120, 135
- Burns, C., Hsiao, E., Suntzeff, N., et al. 2021, *The Astronomer’s Telegram*, 14441, 1
- Childress, M. J., Hillier, D. J., Seitzzahl, I., et al. 2015, *MNRAS*, 454, 3816
- Contreras, C., Phillips, M. M., Burns, C. R., et al. 2018, *ApJ*, 859, 24
- DerKacy, J. M., Ashall, C., Hoeflich, P., et al. 2023, arXiv e-prints, arXiv:2301.03647
- Dimitriadis, G., Sullivan, M., Kerzendorf, W., et al. 2017, *MNRAS*, 468, 3798
- Dolphin, A. 2016, *DOLPHOT: Stellar photometry*, *Astrophysics Source Code Library*, record ascl:1608.013, ascl:1608.013
- Dolphin, A. E. 2000, *PASP*, 112, 1383
- Flörs, A., Spyromilio, J., Taubenberger, S., et al. 2020, *MNRAS*, 491, 2902
- Foley, R. J., Challis, P. J., Chornock, R., et al. 2013, *ApJ*, 767, 57
- Fransson, C., & Jerkstrand, A. 2015, *ApJL*, 814, L2
- Gerardy, C. L., Meikle, W. P. S., Kotak, R., et al. 2007, *ApJ*, 661, 995
- Graham, M. L., Kennedy, T. D., Kumar, S., et al. 2022, *MNRAS*, 511, 3682
- Graur, O., Maguire, K., Ryan, R., et al. 2020, *Nature Astronomy*, 4, 188
- Gupta, S., Caprioli, D., & Haggerty, C. C. 2021, *ApJ*, 923, 208
- Hoeflich, P., Ashall, C., Bose, S., et al. 2021, *ApJ*, 922, 186
- Hosseinzadeh, G., Sand, D. J., Lundqvist, P., et al. 2022, *ApJL*, 933, L45
- Hoyer, N., Neumayer, N., Seth, A. C., Georgiev, I. Y., & Greene, J. E. 2022, arXiv e-prints, arXiv:2212.04151
- Hoyle, F., & Fowler, W. A. 1960, *ApJ*, 132, 565
- Hristov, B., Collins, D. C., Hoeflich, P., Weatherford, C. A., & Diamond, T. R. 2018, *ApJ*, 858, 13
- Hristov, B., Hoeflich, P., & Collins, D. C. 2021, *ApJ*, 923, 210
- Iwamoto, K., Brachwitz, F., Nomoto, K., et al. 1999, *ApJS*, 125, 439
- Jha, S. W., Maguire, K., & Sullivan, M. 2019, *Nature Astronomy*, 3, 706
- Johansson, J., Amanullah, R., & Goobar, A. 2013, *MNRAS*, 431, L43
- Johansson, J., Goobar, A., Kasliwal, M. M., et al. 2017, *MNRAS*, 466, 3442
- Kerzendorf, W. E., McCully, C., Taubenberger, S., et al. 2017, *MNRAS*, 472, 2534
- Kluyver, T., Ragan-Kelley, B., Pérez, F., et al. 2016, in *IOS Press*, 87–90
- Kourkchi, E., & Tully, R. B. 2018, *VizieR Online Data Catalog*, J/ApJ/843/16
- Krisciunas, K., Contreras, C., Burns, C. R., et al. 2017, *AJ*, 154, 211
- Kushnir, D., & Waxman, E. 2020, *MNRAS*, 493, 5617
- Kwok, L. A., Jha, S. W., Temim, T., et al. 2022, arXiv e-prints, arXiv:2211.00038
- Lee, J. C., Sandstrom, K. M., Leroy, A. K., et al. 2022, arXiv e-prints, arXiv:2212.02667
- Leloudas, G., Stritzinger, M. D., Sollerman, J., et al. 2009, *A&A*, 505, 265
- Leroy, A. K., Schinnerer, E., Hughes, A., et al. 2021, *ApJS*, 257, 43
- Li, C., Hillier, D. J., & Dessart, L. 2012, *MNRAS*, 426, 1671
- Maguire, K., Sim, S. A., Shingles, L., et al. 2018, *MNRAS*, 477, 3567
- Maoz, D., Mannucci, F., & Nelemans, G. 2014, *ARA&A*, 52, 107
- Mayker Chen, N., Leroy, A. K., Lopez, L. A., et al. 2022, arXiv e-prints, arXiv:2212.09766
- Mazzali, P. A., Sullivan, M., Filippenko, A. V., et al. 2015, *MNRAS*, 450, 2631
- Mazzali, P. A., Bikmaev, I., Sunyaev, R., et al. 2020, *MNRAS*, 494, 2809
- McClelland, C. M., Garnavich, P. M., Milne, P. A., Shappee, B. J., & Pogge, R. W. 2013, *ApJ*, 767, 119
- Milne, P. A., The, L. S., & Leising, M. D. 2001, *ApJ*, 559, 1019

- Monard, L. A. G. 2010, Central Bureau Electronic Telegrams, 2334, 1
- Pankey, Titus, J. 1962, PhD thesis, Howard University, Washington DC
- Peltonen, J., et al. in prep., MNRAS
- Penney, R., & Hoefflich, P. 2014, ApJ, 795, 84
- Perrin, M. D., Long, J., Sivaramakrishnan, A., et al. 2015, WebbPSF: James Webb Space Telescope PSF Simulation Tool, Astrophysics Source Code Library, record ascl:1504.007, ascl:1504.007
- Pinto, P. A., & Eastman, R. G. 2000, ApJ, 530, 757
- Remming, I. S., & Khokhlov, A. M. 2014, ApJ, 794, 87
- Rieke, G. H., Ressler, M. E., Morrison, J. E., et al. 2015, PASP, 127, 665
- Rieke, M. J., Kelly, D. M., Misselt, K., et al. 2022, arXiv e-prints, arXiv:2212.12069
- Rigby, J., Perrin, M., McElwain, M., et al. 2022, arXiv e-prints, arXiv:2207.05632
- Rodrigo, C., & Solano, E. 2020, in XIV.0 Scientific Meeting (virtual) of the Spanish Astronomical Society, 182
- Schmidt, B. P., Suntzeff, N. B., Phillips, M. M., et al. 1998, ApJ, 507, 46
- Seitenzahl, I. R., Taubenberger, S., & Sim, S. A. 2009, MNRAS, 400, 531
- Shappee, B. J., Stanek, K. Z., Kochanek, C. S., & Garnavich, P. M. 2017, ApJ, 841, 48
- Shingles, L. J., Flörs, A., Sim, S. A., et al. 2022, MNRAS, 512, 6150
- Shingles, L. J., Sim, S. A., Kromer, M., et al. 2020, MNRAS, 492, 2029
- Siebert, T., Diehl, R., Khachatryan, G., et al. 2016, A&A, 586, A84
- Stanishev, V., Goobar, A., Benetti, S., et al. 2007, A&A, 469, 645
- Stritzinger, M., & Sollerman, J. 2007, A&A, 470, L1
- Tartaglia, L., Sand, D. J., Valenti, S., et al. 2018, VizieR Online Data Catalog, J/ApJ/853/62
- Telesco, C. M., Höflich, P., Li, D., et al. 2015, ApJ, 798, 93
- Tucker, M. A., Ashall, C., Shappee, B. J., et al. 2022a, ApJL, 926, L25
- Tucker, M. A., Shappee, B. J., Kochanek, C. S., et al. 2022b, MNRAS, 517, 4119
- Valenti, S., Sand, D. J., Wyatt, S., et al. 2021, Transient Name Server Discovery Report, 2021-3864, 1
- Weisz, D., et al. in prep., ApJ
- Wells, M., Pel, J. W., Glasse, A., et al. 2015, PASP, 127, 646
- Wilk, K. D., Hillier, D. J., & Dessart, L. 2020, MNRAS, 494, 2221
- Williams, K. A., Hermes, J. J., & Vanderbosch, Z. P. 2022, AJ, 164, 131
- Wolf, C., Onken, C. A., Luvaul, L. C., et al. 2018, PASA, 35, e010
- Wright, G. S., Wright, D., Goodson, G. B., et al. 2015, PASP, 127, 595